Fiber-optic probe for noninvasive real-time determination of tissue optical properties at multiple wavelengths

Dam, J. S; Pedersen, C. B; Dalgaard, T; Fabricius, P. E; Aruna, P; Andersson-Engels, Stefan

Link to publication

Fiber-optic probe for noninvasive real-time determination of tissue optical properties at multiple wavelengths

Jan S. Dam, Carsten B. Pedersen, Torben Dalgaard, Paul Erik Fabricius, Prakasa Aruna, and Stefan Andersson-Engels

We present a compact, fast, and versatile fiber-optic probe system for real-time determination of tissue optical properties from spatially resolved continuous-wave diffuse reflectance measurements. The system collects one set of reflectance data from six source–detector distances at four arbitrary wavelengths with a maximum overall sampling rate of 100 Hz. Multivariate calibration techniques based on two-dimensional polynomial fitting are employed to extract and display the absorption and reduced scattering coefficients in real-time mode. The four wavelengths of the current configuration are 660, 785, 805, and 974 nm, respectively. Cross-validation tests on a 6×7 calibration matrix of Intralipid–dye phantoms showed that the mean prediction error at, e.g., 785 nm was 2.8% for the absorption coefficient and 1.3% for the reduced scattering coefficient. The errors are relative to the range of the optical properties of the phantoms at 785 nm, which were 0–0.3/cm for the absorption coefficient and 6–16/cm for the reduced scattering coefficient. Finally, we also present and discuss results from preliminary skin tissue measurements. © 2001 Optical Society of America

OCIS codes: 170.1470, 170.1580, 170.3890, 170.6510.

1. Introduction

The optical properties of human tissue,[1] i.e., the absorption coefficient μ_a, the scattering coefficient μ_s, and the anisotropy factor g, may provide important information on the composition and the physiological dynamics of the tissue. Whereas μ_a may provide information on tissue chromophores,[2–4] μ_s and g may be used to characterize the form, size, and concentration of various scattering components in the tissue.[5–8]

Owing to the obvious advantages of noninvasive and minimally invasive measurements, determination of tissue optical properties based on diffuse reflectance measurements has a significant potential in biomedical diagnostics and monitoring. Diffuse reflectance measurements may be roughly divided into time-resolved[9,10] (TR), frequency-domain[11,12] (FD),

and spatially resolved continuous-wave[13–21] (cw) methods. Traditionally, TR- and FD-based methods have been considered to be more accurate for absolute determination of optical properties than cw based methods. However, TR and FD methods also require more bulky and expensive equipment, and a larger sample volume, which may restrict some biomedical applications, e.g., implementation in portable monitoring equipment or in endoscopes and catheters. Recent research[19] has shown that cw-based methods may yield absolute determination of the optical properties of tissue with accuracies similar to the TR and FD methods, which makes cw-based methods a better choice for many practical applications.

Continuous-wave diffuse reflectance methods may be further divided into methods based on probes in contact with the tissue and noncontact methods, i.e., image reflectometry. The latter method is advantageous in clinical applications because of the noncontact and thus sterile properties. The advantage of contact probes is that they can be made small and portable. Therefore they are well suited for (a) optical biopsies of body cavities or organs, because a probe may be implemented in existing endoscopic equipment, or (b) for long-time monitoring of tissue optical properties, because the probe may be fixed to the skin and still allow the patient to move around.

J. S. Dam (jan.sorensen_dam@fysik.lth.se), C. B. Pedersen, T. Dalgaard, and P. E. Fabricius are with Bang & Olufsen Medicom a/s, DK-7600, Struer, Denmark. S. Andersson-Engels is with the Department of Physics, Lund Institute of Technology, P.O. Box 118, SE-22100, Lund, Sweden. P. Aruna is with Anna University, 600 025 Madras, India.
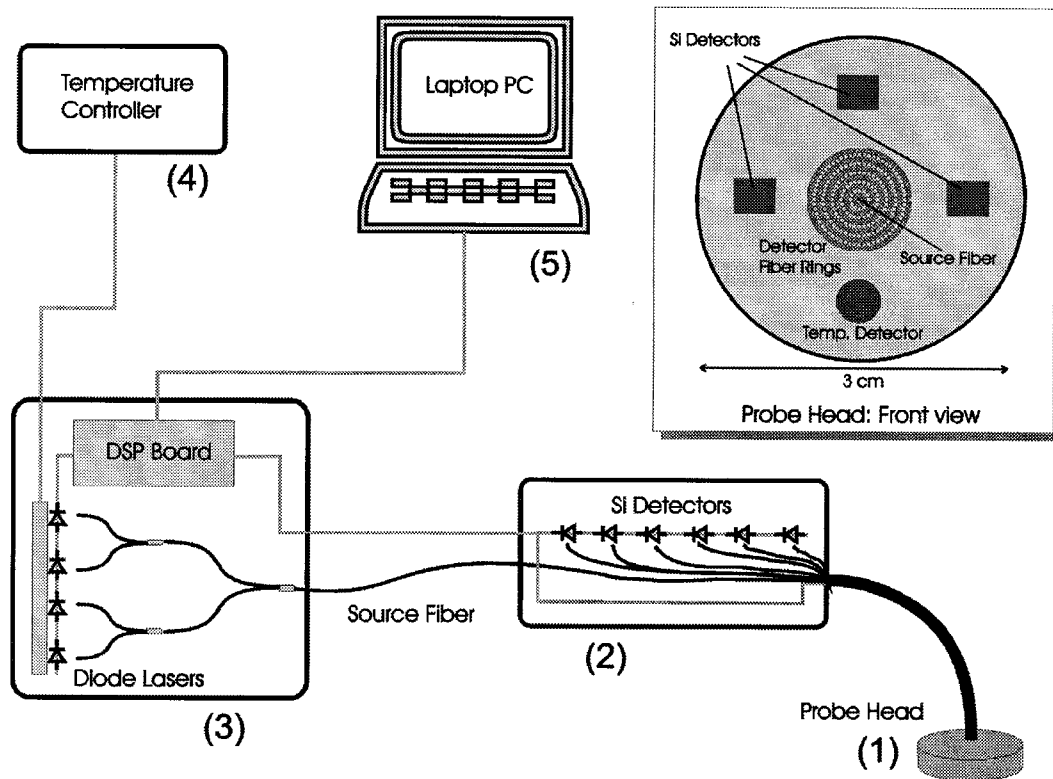
Fig. 1. Diagram of the fiber-optic system for $R(r)$ measurements applied in this paper. (1) Probe head with source and detector optical fibers mounted in a rotational symmetric configuration. (2) Handheld box with silicon photodiodes and amplifier electronics. (3) Stationary box containing a digital signal processing (DSP) board and the light sources in the form of diode lasers. (4) External temperature controller to maintain a constant temperature of the diode lasers. (5) Laptop PC to analyze, display, and store the acquired $R(r)$ data.

However, there are a number of drawbacks related to skin tissue monitoring using a contact probe system. First, the static mechanical pressure of the probe may influence the tissue optical properties, e.g., by displacement of blood in the sample volume. Second, physical activities of the patient may lead to motion artifacts, i.e., movements of the probe relative to the skin tissue. Finally, obstruction of the tissue and sweating may cause long-term changes in the tissue optical properties and the probe–skin optical interface. All such contributions have to be isolated to extract the relevant information from diffuse reflectance measurements.

Accurate closed-form mathematical analytical expressions for spatially resolved diffuse cw reflectance $R(r)$ as a function of the optical properties are strongly limited by requirements to the range of the optical properties and the specific geometry of the setup.[22] Therefore methods based on more-accurate numerical light-propagation models, e.g., Monte Carlo simulations,[23] are often used in conjunction with various forms of multivariate analysis[19,24] to solve the inverse problem of extracting the optical properties from $R(r)$ measurements. However, as a consequence of the similarity principle,[25,26] normally only μ_a and the reduced scattering coefficient $\mu_s' = (1 - g)\mu_s$ are extracted from $R(r)$ measurements.

In this paper we present a fiber-optic probe system for *in vivo* real-time determination of tissue optical properties based on $R(r)$ measurements at four arbitrary wavelengths. The probe system collects the diffuse reflectance at six distances, extracts the corresponding μ_a and μ_s', and displays the results immediately on a laptop personal computer (PC). The prediction of μ_a and μ_s' is based on multiple polynomial regression[27] and calibration on a set of Intralipid–dye phantoms with well-known optical properties within a range typical for biologic tissue[28] in the visible and the near-infrared regions. In the following sections we first give a description of the probe specifications and the principles of the calibration and prediction algorithms. Next, we present and discuss the results obtained from phantom measurements and simulated numerical tests with respect to prediction errors, robustness, and the like. Finally, we present the results of preliminary prediction tests obtained from a series of clinical measurements on normal skin tissue.

2. Materials and Methods

A. Fiber Probe System

Figure 1 shows the basics of the fiber probe system we used for the measurements described below. The

system consists of a probe head with a 200-μm source fiber in the center surrounded by five equally spaced concentric rings of 250-μm detector fibers. We chose this ring geometry instead of, e.g., a simpler linear geometric configuration, in part to be able to collect more light at farther distances and in part to minimize any problems arising from tissue inhomogeneities during clinical measurements. The fibers of each single ring detector are bundled and terminated on separate silicon photodiodes. In addition, three photodiodes and a temperature sensor are mounted directly near the perimeter of the probe head. Thus $R(r)$ can be collected at six distances, in part at the five fiber rings (r = 0.6, 1.2, 1.8, 2.4, and 3.0 mm) and in part at the directly mounted photodiodes (r = 7.8 mm). These distances were chosen on the basis of previous studies.[19] The gain of each reflectance detector was calibrated in an integrating sphere setup to obtain equal outputs at constant input light intensities. The source fiber is coupled into four separate fibers, each connected to four replaceable low-power diode lasers. The diode lasers are mounted on a heat sink with a constant temperature maintained by an external controller. Furthermore, a separate reference detector monitors the output of the source fiber at the probe head. The diode lasers may be selected arbitrarily to suit different applications. In this paper we used diode lasers with the wavelengths 660, 785, 805, and 974 nm, which are well suited for applications involving hemodynamic monitoring. The data acquisition and storage is controlled by a laptop PC connected to a digital signal processing (DSP) board. In each $R(r)$ measurement the detector hardware collects data simultaneously in eight parallel channels from the probe head, i.e., from the six detector rings, from the reference detector at the source fiber, and from the temperature sensor. One cycle of four successive measurements (i.e., one at each wavelength) including dark measurements may be performed in ~10 ms; thus the maximum sampling rate of the system is ~100 Hz. To minimize any interference from background light or drift of the light source, the dark measurements are subtracted from the measured reflectance data after which they are normalized relative to the source reference. The DSP board accomplishes this prior to when the data are analyzed, displayed, and stored by the PC.

B. Calibration and Prediction Algorithms

In theory, μ_a and μ_s' may be determined with $R(r)$ data from only two of the six detector distances of the fiber probe. Building on our previous research,[19,27] we thus applied multiple polynomial regression (MPR) to create a calibration model and subsequently extract μ_a and μ_s' from $R(r)$ measurements at r_1 = 0.6 mm and at r_2 = 7.8 mm. For the sake of clarity we give a summary of the MPR method here. We first measure $R(r)$ at r_1 and at r_2 for a set of calibration samples with well-defined optical properties and de-

note them $R_{1,\text{cal}}$ and $R_{2,\text{cal}}$. Then we find a double-polynomial fit to $R_{1,\text{cal}}$ and $R_{2,\text{cal}}$:

$$R_{1,\text{fit}}(\mu_a, \mu_s', m) = (a_0 + a_1\mu_a + a_2\mu_a{}^2 + \ldots a_m\mu_a{}^m)$$
$$\times (b_0 + b_1\mu_s'^2 + \ldots b_m\mu_s'^m),$$

$$R_{2,\text{fit}}(\mu_a, \mu_s', m) = (c_0 + c_1\mu_a + c_2\mu_a{}^2 + \ldots c_m\mu_a{}^m)$$
$$\times (d_0 + d_1\mu_s'^2 + \ldots d_m\mu_s'^m), \quad (1)$$

Where a, b, c, and d are fitting coefficients determined by least-squares regression. $R_{1,\text{fit}}$ and $R_{2,\text{fit}}$ thus constitute the calibration model. The next step is to solve the inverse problem of determining μ_a and μ_s' from $R(r)$ measurements on a set of prediction samples, i.e., $R_{1,\text{meas}}$ and $R_{2,\text{meas}}$. First we define

$$F(\mu_a, \mu_s') = R_{1,\text{fit}} - R_{1,\text{meas}},$$

$$G(\mu_a, \mu_s') = R_{2,\text{fit}} - R_{2,\text{meas}}. \quad (2)$$

Then we use a Newton–Raphson algorithm to perform converging iterative calculations of μ_a and μ_s':

$$-\begin{bmatrix} \mathbf{F}(\mu_{a,k}, \mu_{s,k}') \\ \mathbf{G}(\mu_{a,k}, \mu_{s,k}') \end{bmatrix} = \begin{bmatrix} \dfrac{\partial F}{\partial \mu_a} & \dfrac{\partial F}{\partial \mu_s'} \\ \dfrac{\partial G}{\partial \mu_a} & \dfrac{\partial G}{\partial \mu_s'} \end{bmatrix} \begin{pmatrix} h_{a,k} \\ h_{s,k} \end{pmatrix}$$

$$\begin{pmatrix} \mu_{a,k+1} \\ \mu_{s,k+1}' \end{pmatrix} = \begin{pmatrix} \mu_{a,k} \\ \mu_{s,k}' \end{pmatrix} + \begin{pmatrix} h_{a,k} \\ h_{s,k} \end{pmatrix}$$

$$k = 0, 1, 2, 3, \ldots, \quad (3)$$

where k is an index and h_a and h_s are correction terms of μ_a and μ_s' The iterations were stopped when both h_a and $h_s < 1 \times 10^{-6}$ (cm^{-1}). With such strict criteria, previous research[27] showed that the contribution of the Newton–Raphson method to the total prediction error was negligible.

Since in this study we want to extract two optical properties only, i.e., μ_a and μ_s', the MPR method implies exactly two input variables as well, i.e., $R(r_1)$ and $R(r_2)$. However, owing to tissue inhomogeneity and/or noisy measurement conditions, it might be advantageous to include more source–detector distances during measurements and then subsequently apply some sort of dimension-reduction method before the data are fed into the MPR method. To test such a procedure, we also applied principal component analysis (PCA) on the data from all six source–detector distances of the probe system and then used the resulting two main principal components P_1 and P_2 as input to the MPR method instead of $R(r_1)$ and $R(r_2)$.

All the prediction algorithms we applied in this paper were implemented in Matlab and run on a 166-MHz PC. With this configuration, the prediction of a single set of μ_a and μ_s' could be performed in ~60 ms.

Table 1. Optical Property Ranges of 6×7 Matrix of Intralipid–Ink Phantoms Determined from Integrating Sphere Measurements

	Optical Property Range (cm^{-1})	
λ (nm)	μ_a	$\mu_s{}'$
660	0–0.36	7.3–19.5
785	0–0.32	6.1–16.3
805	0–0.31	6.0–16.0
974	0.45–0.68	4.8–12.7

C. Phantoms

Because of the unknown numerical apertures of the fiber probe light source and detectors, we chose to calibrate the system directly on a set of phantoms instead of using a mathematical light-propagation model. The phantoms consisted of well-defined aqueous solutions of Intralipid and black ink in cylindrical glass containers with a diameter of 10 cm and a height of 4 cm. We determined the scattering and absorption spectra of the Intralipid and the black ink from integrating sphere[27] and traditional transmission spectroscopy measurements. On the basis of these spectra, we mixed a 6×7 matrix of phantoms with μ_a and $\mu_s{}'$ ranges typical for skin tissue (see Table 1). The applied ranges of Intralipid concentrations were 0.6, 0.8, . . . , 1.6%, and the range of the ink concentrations were 0.0, 0.2, . . . , 1.2%. It should be noted that the absorption of pure ink is much higher than that of typical biologic substances; thus the ink concentrations in the following refers to a premixed basic ink–water solution with a biologically relevant absorption level. To perform the prediction experiments, we calibrated the probe system directly to the concentrations of the Intralipid and the ink in the phantoms, assuming that both the absorption of pure Intralipid[29,30] and the scattering of the ink were negligible. At 660, 785, and 805 nm we assumed that the background absorption was negligible as well. However, water exhibits substantial absorption[31] at 974 nm ($\mu_{a,\text{water}} = 0.45$ cm^{-1}). This was incorporated in the concentration-to-absorption tabulation by assuming a constant water absorption contribution at this particular wavelength (i.e., $c_{\text{ink}} = 0\% \Rightarrow \mu_a = 0.45$ cm^{-1}).

3. Results

Once the 6×7 matrix of phantoms was mixed, we determined the actual optical properties of a subset of the phantom matrix, using integrating sphere measurements. Figure 2(a) shows the mean absorption spectra of the six phantoms with 1% ink concentrations but varying Intralipid concentrations, and Fig. 2(b) shows the mean scattering spectra of the seven phantoms with 1% Intralipid concentrations but varying ink concentrations. We used the results from Fig. 2(a) to relate the concentrations of Intralipid and ink to the optical properties of the phantoms. The resulting optical property ranges of the 6×7 matrix phantoms are listed in Table 1.
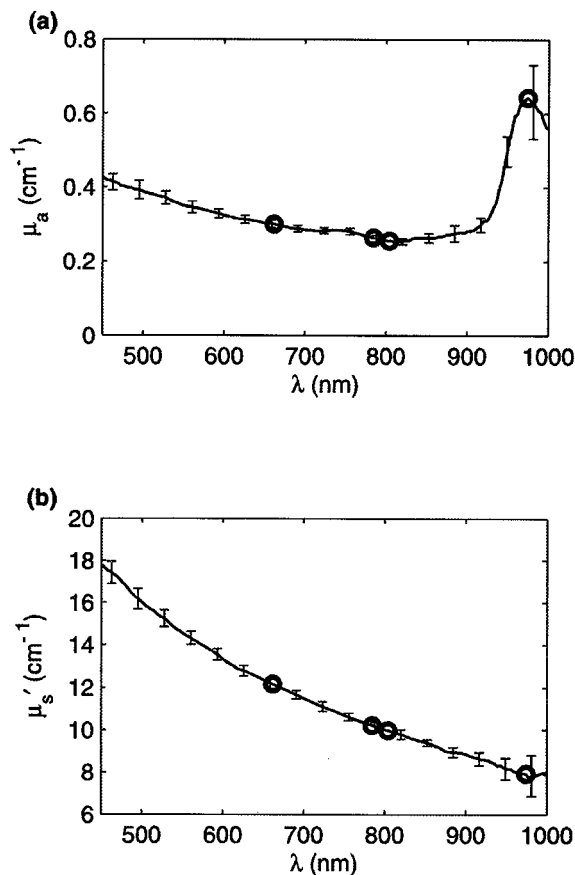
Figures 3(a) and 3(b) show the measured intensity

Fig. 2. Optical property spectra of the applied Intralipid–ink phantoms. (a) Mean of μ_a as a function of the wavelength λ for the six phantoms with 1% ink concentration but varying Intralipid concentrations. (b) Mean of $\mu_s{}'$ as a function of the wavelength for the seven phantoms with 1% Intralipid concentration but varying ink concentrations. The error bars of the spectra in panels (a) and (b) show the standard deviations of μ_a and $\mu_s{}'$, respectively. The circles indicate the values at the four wavelengths of the probe. The two spectra were measured and calculated with an integrating sphere setup in conjunction with the MPR method.

$R(r)$ at 785 nm as a function of μ_a and $\mu_s{}'$ at $r = 0.6$ mm and $r = 7.8$ mm, respectively. Corresponding plots at the three remaining wavelengths of the probe, i.e., 660, 805, and 974 nm, showed similar characteristics; i.e., they were also smooth and monotonic, which suggests that they may be fitted well by Eq. (1) with relatively low-order polynomials. Preliminary experiments showed that using Eq. (1) with $m = 3$ provided the best overall calibration model, concerning accuracy and robustness. The prediction accuracy of the MPR method was tested with leave-one-out cross validation. This means that we successively performed predictions with the data from one phantom for prediction and the data from the remaining 41 phantoms of the 6×7 matrix for calibration. To ensure that all $R(r)$ variations were covered by the calibration models, we carried out predictions only on the 4×5 interior subset of the 6×7 matrix. Table 2 presents the results from these cross-validation prediction tests.
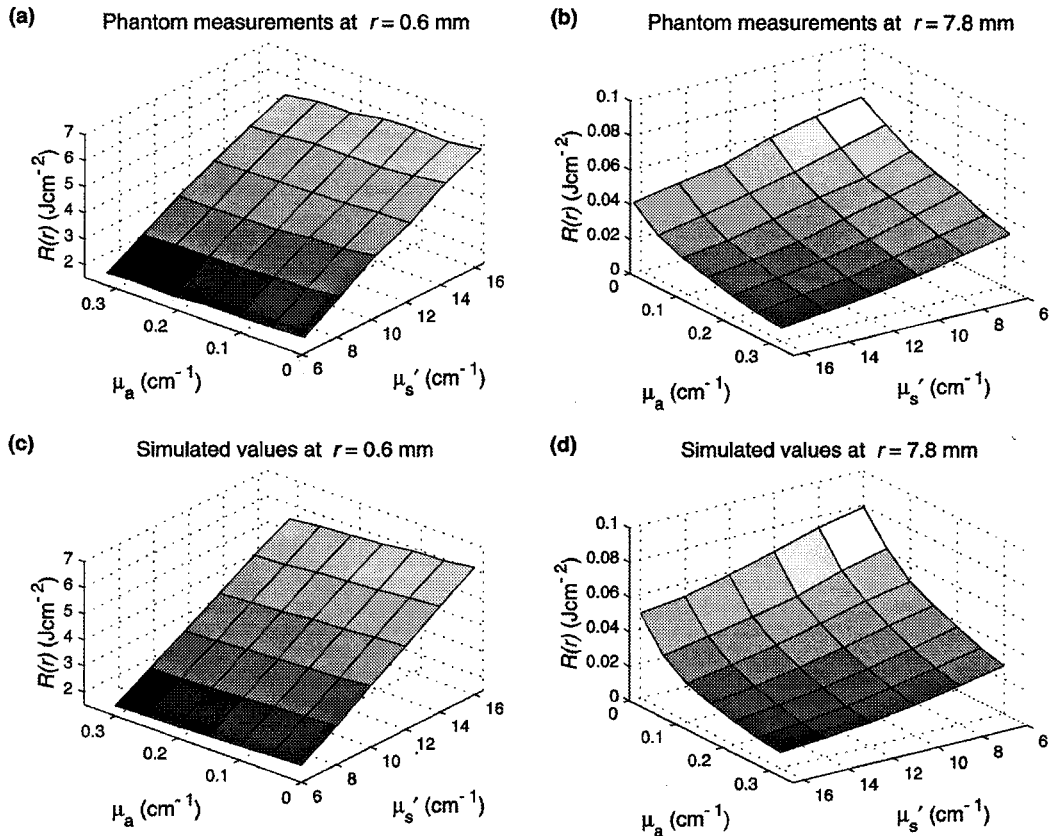
Fig. 3. Surface plots of $R(r)$ at $r_1 = 0.6$ mm and $r_2 = 7.8$ mm as a function of μ_a and μ_s'. Panels (a) and (b) show the $R(r)$ plots of the 6×7 Intralipid phantoms at 785 nm, and panels (c) and (d) show the corresponding $R(r)$ plots based on Monte Carlo simulations. Note that the arbitrary intensity units of measured $R(r)$ plots have been scaled in order to compare them with the simulated plots.

To check our experimental results, and to examine the robustness, noise sensitivity, and so on, of the applied calibration model and prediction algorithms, we also performed a series of numerical tests based on Monte Carlo simulations with a geometric configuration analogous to the fiber probe setup described in Subsection 3.A. However, unlike the measurements, the simulations were based on a collimated incident beam, a semi-infinite medium, and ½π acceptance angle for collection of the diffuse reflectance. The tests were carried out as follows: (I) First, we generated a basic 6×7 calibration matrix with optical properties corresponding to the 6×7 phantom

matrix at $\lambda = 785$ nm and then performed prediction tests similar to the phantom cross-validation tests described above. Figure 4 shows a selected set of $R(r)$ profiles from these simulations [see also Figs. 3(c) and 3(d)]. (II) Next, to test the algorithms with independent calibration and prediction data, we generated a series of 20 $R(r)$ data sets with random μ_a and μ_s' distributions and then performed predictions on this randomized set with a calibration model based on the full 6×7 basic matrix. (III) The basic 6×7 matrix was generated with 1×10^6 photons. To examine the impact of random measurement noise on the prediction performance, we generated a second 6×7 matrix with less noise by using 1×10^7 photons and performed identical cross-validation tests on this set. (IV) We also wanted to investigate the effect of using a calibration model with a higher μ_a and μ_s' resolution; thus we also carried out cross-validation tests on a 11×13 calibration matrix with the same μ_a and μ_s' range and number of photons as the basic 6×7 matrix. (V) Finally, we tested the effect of using PCA for dimension reduction as described in Subsection 3.B. The resulting mean and maximum prediction errors from the numerical tests (I–V) described above are summarized in Fig. 5.

To validate the optical property range of the applied calibration model, we performed a series of

Table 2. Leave-One-Out Cross-Validation Prediction Tests Based on Phantom Measurements[a]

	Prediction Errors (%)			
	μ_a		μ_s'	
λ (nm)	Mean	Max	Mean	Max
600	3.3 (2.5)	18 (6.7)	1.7 (1.7)	3.7 (4.0)
785	2.8	8.3	1.3	3.4
805	2.6	9.0	1.5	4.2
974	3.7	9.7	1.6	3.8

[a]The errors are relative to the ranges of μ_a and μ_s' of the phantoms. The bracketed values at $\lambda = 660$ nm have been corrected for an outlier detected by visual inspection of the measured $R(r)$ data.
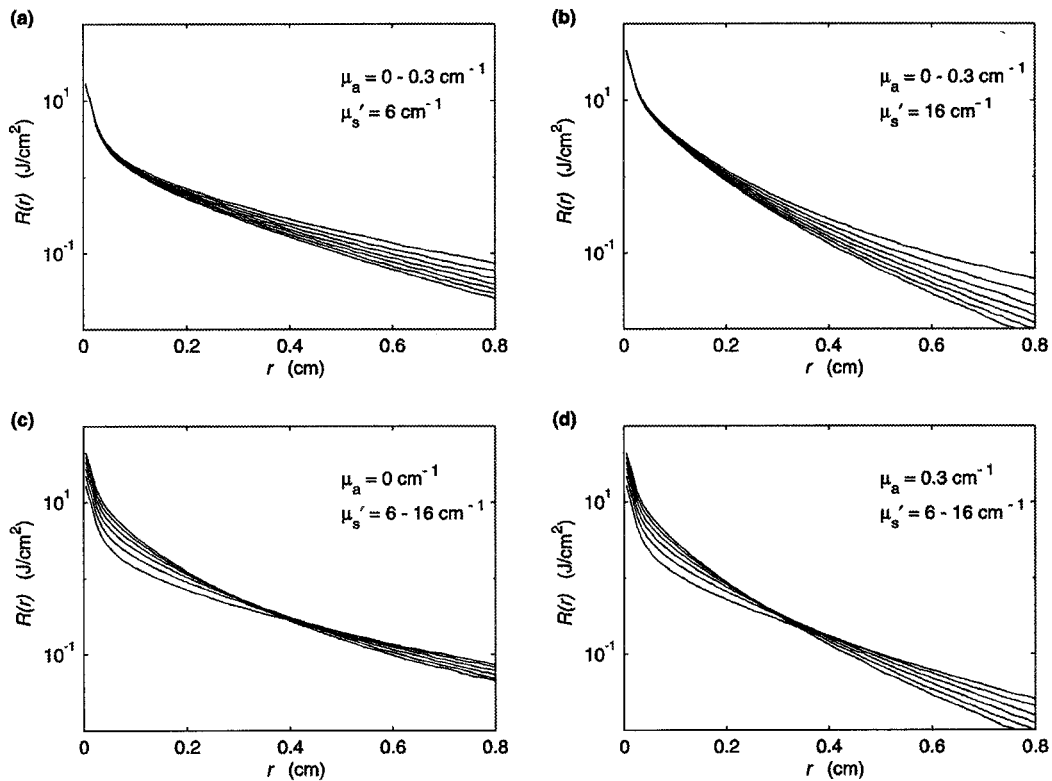
Fig. 4. Monte Carlo simulated $R(r)$ data for various combinations of μ_a and μ_s' within ranges typical for skin tissue at 785 nm. In (a) and (b), μ_s' is kept constant at 6 cm^{-1} and 16 cm^{-1}, respectively while μ_a is varied within the range 0–0.3 cm^{-1}. In (c) and (d) μ_a is kept constant at 0 cm^{-1} and 0.3 cm^{-1}, respectively, whereas μ_s' is varied within the range 6–16 cm^{-1}.

probe measurements on the inner forearm of five healthy individuals. Figure 6 shows how the mean $R(r)$ of all five individuals (circles) at each probe distance is situated relative to the $R(r)$ ranges of the calibration model (vertical bars). Figure 6 also shows the predicted optical properties at all four wavelengths calculated from the mean $R(r)$ data with Eq. (1)-(3). It can be seen that the measured skin tissue at $\lambda = 660$ nm and $r = 7.8$ mm is outside the calibration model range, and therefore it is not possible to predict μ_a and μ_s' correctly in this case.

4. Discussion

A. Geometry Considerations

In Fig. 4(a) and 4(b) μ_s' is kept constant at values of 6 and 16 cm^{-1}, respectively. In these two cases, it appears that changes in μ_a have a negligible effect on $R(r)$ at distances close to the source. In Figs. 4(c) and 4(d), μ_a is kept constant at values of 0 and 0.3 cm^{-1}, respectively. Here it is notable that there is very little variation in $R(r)$ at $r \approx 0.35$ cm in Fig. 4(c) and at $r \approx 0.3$ in Fig. 4(d). Using a figure of speech, we say that there is a *pivot point* in the $R(r)$ graphs at $r \approx 0.3$ cm, when μ_a is kept constant. The simulations in Figs. 4(a) and 4(b) indicates that μ_s' may be determined with good accuracy from close distance measurements only. To determine μ_a as well, Figs. 4(c) and 4(d) suggest that $R(r)$ measurements close to the pivot point should be included, since there is little

variation in $R(r)$ as a function of μ_s' at this point. Although, other authors[32,33] support this argument, we based our experiments in this paper on close range distances in conjunction with distances well beyond the pivot point. We did this because our previous studies[19] showed that this geometrical configuration provided a better accuracy than a configuration with close range distances in conjunction with distances near the pivot point.

B. Phantom Measurements

The prediction tests using Intralipid–ink phantoms show a good accuracy (see Table 2). The mean prediction errors at all four wavelengths is roughly 3% for μ_a, and 1.5% for μ_s', whereas the maximum prediction errors for μ_a and μ_s' are approximately 11% and 4%, respectively. The prediction algorithm converged in all cases; however, the maximum error of μ_a at $\lambda = 660$ nm is remarkably high (18%). A visual inspection of the raw $R(r)$ data at 660 nm revealed an outlier at $r = 7.8$ mm in one of the phantom measurements. This outlier could be due to an air bubble or a piece of dirt at one of the three 7.8-mm detectors in this particular measurement. When we removed the outlier from the calibration and prediction analysis at $\lambda = 660$ nm, we obtained the improved results shown in brackets in Table 2. In general, the prediction errors of μ_a are approximately twice as high as the errors of μ_s'. This may be attributed in part to the fact that μ_a is mainly deter-
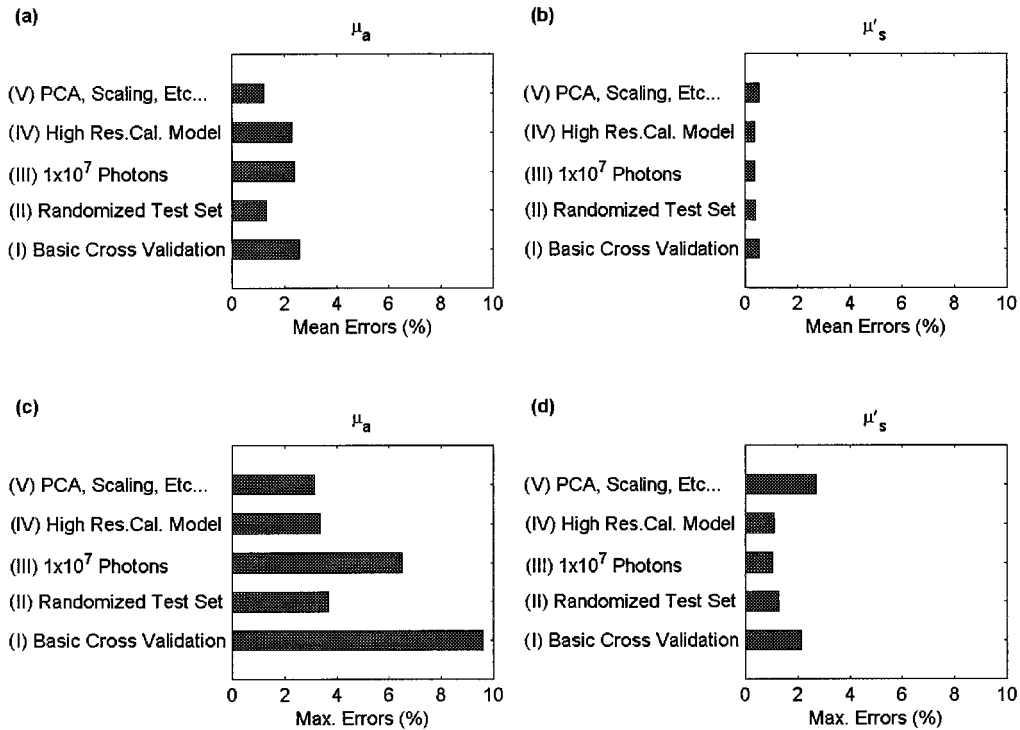
Fig. 5. Various numerical tests on Monte Carlo simulated $R(r)$ data. Panels (a) and (b) show the mean prediction errors of μ_a and μ_s', respectively. Panels (c) and (d) show the corresponding maximum prediction errors. From below: (I) cross validation on a basic 6×7 calibration matrix (10^6 photons) corresponding to phantom measurements at 785 nm, (II) predictions on data with random μ_a and μ_s' distribution, (III) cross validation on 6×7 matrix generated with 1×10^7 photons, (IV) cross validation on a high-resolution 11×13 calibration matrix, (V) cross validation on the basic 6×7 calibration matrix with principal component analysis.

mined on the basis of the $R(r)$ data at $r = 7.8$ mm, whereas μ_s' is almost solely determined from $R(r)$ data at $r = 0.6$ mm, where the signal level is ~1000 times the level at $r = 7.8$ mm. The μ_a predictions are therefore more sensitive to any background noise interference during the measurements.

With reference to the comments on the pivot point in Subsection 5.A we also performed a series of prediction tests, in which we replaced the $R(r)$ probe data at $r_2 = 7.8$ mm with probe data at the pivot point $r_{pivot} = 3.0$ mm. This had no significant effect on the μ_s' prediction errors, but both the mean and the maximum μ_a prediction errors increased ~30% compared with results reported in Table 2.

C. Numerical Tests

The general shape of the measured and the simulated $R(\mu_a, \mu_s')$ plots in Fig. 3 are very similar at corresponding detector distances. However, the simulated plots do show slightly higher $R(\mu_a, \mu_s')$ levels for low μ_a and μ_s' values at $r = 7.8$ mm. This difference is severe enough to prevent the direct use of a calibration model based on Monte Carlo simulations for prediction analyses of $R(r)$ data collected with the fiber probe. The difference between the simulated and the measured $R(r)$ data in Figs. 3(b) and 3(d) may be attributed to the different numerical apertures of the sources and the detectors in the two cases; e.g., the Monte Carlo simulations employ a

collimated source beam, whereas the probe source beam is divergent.

The μ_a prediction errors of the simulated data shown in Figs. 5(a) and 5(c) are comparable with the errors of the measured data Table 2, whereas the μ_s' prediction errors of the simulated data [Figs. 5(b) and 5(d)] are lower than the errors of the measured data. In both cases the μ_a prediction errors are significantly higher than the μ_s' errors, probably owing to the noise sensitivity at $r = 7.8$ mm as discussed above. Figure 5 also shows a drop in the prediction errors when a randomized prediction data set is used. This may be because the quality of the calibration model fit during leave-one-out cross validation is reduced in the vicinity of the μ_a and μ_s' to be predicted.

From Fig. 5 it also appears that a reduction in measurement noise (i.e., more photons) or use of a calibration model with a higher μ_a and μ_s' resolution in both cases lead to a significant drop in maximum prediction errors, whereas the effect on the mean prediction errors is moderate. Finally, it can be seen from Fig. 5 that the use of PCA before calibration and prediction has a positive effect on the μ_a prediction errors, whereas the μ_s' prediction errors are slightly increased. In summary, the prediction accuracies obtained from calibration and prediction on phantoms are comparable with the accuracies obtained from calibration and prediction on Monte Carlo simulated data. The numerical tests suggest that the
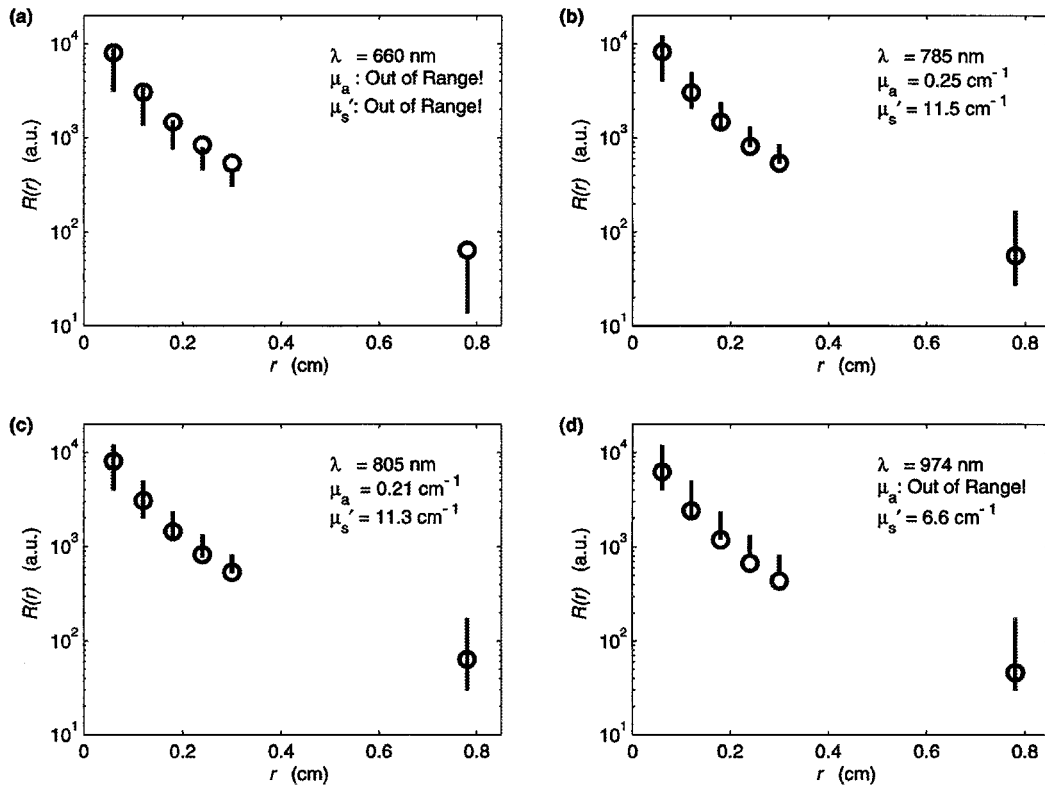
Fig. 6. Mean optical properties at all four wavelengths determined from $R(r)$ measurements on the forearm of five healthy individuals. The vertical bars indicate the valid range of the applied calibration model at various distances and wavelengths, and the circles indicate the mean measured $R(r)$ of the five individuals. At each of the four wavelengths, the stated values of μ_a and μ_s' were determined on the basis of the mean $R(r)$ values at $r_1 = 0.6$ mm and $r_2 = 7.8$ mm.

prediction accuracy may be improved slightly by use of more samples during creation of the calibration model. However, the improvements may hardly justify the additional efforts of creating more calibration phantoms.

D. Clinical Measurements

From Fig. 6 it appears that the range of calibration model covers the span of the measured tissue $R(r)$ data in most cases, except at $\lambda = 660$ nm. At this wavelength the mean of the measured $R(r)$ at $r_2 = 7.8$ mm is above the range of the calibration model. This suggests that either μ_a or μ_s' (or both) of the skin tissue is lower than the minimum values of the calibration model. In the case of μ_a this is not possible, since the model range at $\lambda = 660$ nm is $0-0.36$ cm^{-1}. The minimum value of μ_s' of the model at this wavelength is 7.3 cm^{-1}, and it is not likely that the measured μ_s' should be beneath this limit either. At the three remaining wavelengths the measured $R(r)$ at $r_1 = 0.6$ mm and $r_2 = 7.8$ mm are within the limits of the calibration mode, and the extracted μ_a or μ_s' shows a reasonable correlation with other studies.[20,34] However, at 974 nm, it appears that the measured $R(r)$ data, at some of the intermediate distances (i.e., at $r = 2.4$ and 3.0 mm), are not within the ranges of the calibration model; i.e., the shape of the tissue $R(r)$ profiles are different from the shape of phantom profiles. There may be several reasons for this. First,

in contrast to the phantoms, the volume of the skin tissue sampled by the probe is not homogeneous but basically consists of distinct layers, i.e., the stratum corneum, the vivid epidermis, the epidermis, and so on, Each of these layers has specific optical properties, and therefore the predicted values of μ_a or μ_s' in Fig. 6 are a compound of the optical properties of each separate layer. Second, the ratio of the refractive indices between the probe and the sample (n_{probe}/n_{sample}) is different in the two cases; i.e., $n_{tissue} \approx 1.40$ (Ref. 35) and $n_{phantom} \approx 1.33$. Finally, the probe–tissue interface may not have been optimal, which in turn may lead to light piping effects between the probe and the stratum corneum. Such effects may cause an increase of the farther $R(r)$ values relative to the values close to the light source, which also might explain the out-of-range problems encountered at $\lambda = 660$ nm. To summarize, it is essential to ensure a proper optical contact and apply a uniform and reproducible mechanical pressure in order to obtain valid predictions from contact probe measurements.

E. Acquisition and Analysis Speed

As stated in Subsection 3.A, the maximum acquisition rate of the fiber probe system for all four wavelengths is ~100 Hz, which is sufficient for analyzing the optical property dynamics of most physiological systems. The current software implementation of the prediction algorithms leads to an analysis time

for one set of μ_a or μ_s' of ~50 ms, i.e., an analysis rate of 5 Hz when all four wavelengths are included. To match the analysis rate to the acquisition rate of the probe system, the speed of the prediction algorithms may be increased substantially by application of a more contemporary PC and/or by compiling the algorithms in, e.g., the C programming language.

5. Conclusions

We have demonstrated a versatile, fast, and accurate probe system for real-time noninvasive determination of tissue optical properties from continuous wave (cw) spatially resolved diffuse reflectance measurements. The current calibration of the system was intended to match a typical range of absorption and reduced scattering coefficients of skin tissue, and preliminary clinical trials on a set of healthy individuals showed a good consistency except at $\lambda = 660$ nm. At this wavelength the measured tissue data were outside the range of the calibration model in some instances. This problem may be solved by extension of the calibration model range, but the problem may also originate in the fact that the system was calibrated on homogeneous one-layer phantoms, whereas skin tissue is an inhomogeneous multilayer structure. Furthermore, the clinical trials clearly demonstrated that it is imperative to ensure proper and reproducible refractive-index matching and mechanical contact properties to obtain valid results. All things considered, the system and the method we have presented here provide a sound basis for future development of compact and dedicated systems for noninvasive or minimally invasive medical diagnostics and monitoring. Still, further research is required for exploring the applicability for specific biomedical implementations.

References

1. J. Welch, M. J. C. van Gemert, M. W. Star, and B. C. Wilson, "Overview of tissue optics," *Optical-Thermal Response of Laser-Irradiated Tissue,* A. J. Welch and M. J. C. van Gemert, eds. (Plenum, New York, 1995), Chap. 2.
2. J. W. Feather, D. J. Ellis, and G. Leslie, "A portable reflectometer for the rapid quantification of cutaneous haemoglobin and melanin," Phys. Med. Biol. **33,** 711–722 (1988).
3. S. L. Jacques, "Reflectance spectroscopy with optical fiber devices, and transcutaneous bilirubinometers," in *Biomedical Optical Instrumentation and Laser-Assisted Biotechnology,* A. M. Verga Scheggi, S. Martellucci, A. N. Chester, and R. Pratesi, eds., Vol. E325 of NATO ASI Series (Kluwer Academic, Dordrecht, The Netherlands, 1996), pp. 83–94.
4. M. A. Franceschini, E. Gratton, and S. Fantini, "Noninvasive optical method of measuring tissue and arterial saturation: an application to absolute pulse oximetry of the brain," Opt. Lett. **24,** 829–831 (1999).
5. S. L. Jacques, "Origins of tissue optical properties in the UVA, Visible, and NIR regions," in *Advances in Optical Imaging and Photon Migration*, R. R. Alfano and J. G. Fujimoto, eds., Vol. 2 of OSA Topics in Optics and Photonics Series (Optical Society of America, Washington, D.C., 1996), 364–369.
6. A. H. Hielscher, J. R. Mourant, and I. J. Bigio, "Influence of particle size and concentration on the diffuse backscattering of polarized light from tissue phantoms and biological cell suspensions," Appl. Opt. **36,** 125–135 (1997).
7. J. R. Mourant, J. P. Freyer, A. H. Hielscher, A. A. Eick, D. Shen, and T. M. Johnson, "Mechanisms of light scattering from biological cells relevant to noninvasive optical-tissue diagnostics," Appl. Opt. **37,** 3586–3593 (1998).
8. J. T. Bruulsema, J. E. Hayward, T J. Farrell, M. S. Patterson, L. Heinemann, M. Berger, T. Koschinsky, C. J. Sandahl, H. Orskov, M. Essenpreis, R. G. Schmelzeisen, and D. Bocker, "Correlation between blood glucose concentration in diabetics and noninvasively measured tissue optical scattering coefficient," Opt. Lett. **22,** 190–192 (1997).
9. M. S. Patterson, B. Chance, and B. C. Wilson, "Time resolved reflectance and transmittance for the non-invasive measurement of tissue optical properties," Appl. Opt. **28,** 2331–2336 (1989).
10. S. Andersson-Engels, R. Berg, A. Persson, and S. Svanberg, "Multispectral tissue characterization with time-resolved detection of diffusely scattered white light," Opt. Lett. **18,** 1697–1699 (1993).
11. B. Chance, M. Cope, E. Gratton, N. Ramanujam, and B. Tromberg, "Phase measurement of light absorption and scatter in human tissue," Rev. Sci. Instrum. **69,** 3457–3481 (1998).
12. S. Fantini, M. A. Franceschini, J. S. Maier, S. A. Walker, B. Barbieri, and E. Gratton, "Frequency-domain multichannel optical detector for noninvasive tissue spectroscopy and oximetry," Opt. Eng. **34,** 32–42 (1995).
13. T. J. Farrell, M. S. Patterson, and B. Wilson, "A diffusion theory model of spatially resolved, steady-state diffuse reflectance for noninvasive determination of tissue optical properties *in vivo*," Med. Phys. **19,** 879–888 (1992).
14. P. Marquet, F. Bevilacqua, C. Depeursinge, and E. B. De-Haller, "Determination of reduced scattering and absorption coefficients by a single charge-coupled-device array measurement. I. Comparison between experiments and simulations," Opt. Eng. **34,** 2055–2063 (1995).
15. A. Kienle, L. Lilge, M. S. Patterson, R. Hibst, R. Steiner, and B. C. Wilson, "Spatially resolved absolute diffuse reflectance measurements for noninvasive determination of the optical scattering and absorption coefficients of biological tissue," Appl. Opt. **35,** 2304–2314 (1996).
16. R. Bays, G. Wagnieres, D. Robert, D. Braichotte, J. F. Savary, P. Monnier, and H. van den Bergh, "Clinical determination of tissue optical properties by endoscopic spatially resolved reflectometry," Appl. Opt. **35,** 1756–1766 (1996).
17. J. R. Mourant, T. Fuselier, J. Boyer, T. M. Johnson, and I. J. Bigio, "Predictions and measurements of scattering and absorption over broad wavelength ranges in tissue phantoms," Appl. Opt. **36,** 949–957 (1997).
18. M. G. Nichols, E. L. Hull, and T. H. Foster, "Design and testing of a white-light, steady-state diffuse reflectance spectrometer for determination of optical properties of highly scattering systems," Appl. Opt. **36,** 93–104 (1997).
19. J. S. Dam, P. E. Andersen, T. Dalgaard, and P. E. Fabricius, "Determination of tissue optical properties from diffuse reflectance profiles by multivariate calibration," Appl. Opt. **37,** 772–778 (1998).
20. R. M. Doornbos, L. Lang, R. Alders, F. W. Cross, and H. J. C. M. Sterenborg, "The determination of *in vivo* human tissue optical properties and absolute chromophore concentrations using spatially resolved steady-state diffuse reflectance spectroscopy," Phys. Med. Biol. **44,** 967–981 (1999).
21. T. H. Pham, F. Bevilacqua, T. Spott, J. S. Dam, B. Tromberg, and S. Andersson-Engels, "Quantifying the absorption and reduced scattering coefficients of tissuelike turbid media over a broad spectral range with a noncontact Fourier transform hyperspectral imaging," Appl. Opt. **39,** 6487–6497.

22. L. V. Wang, "Source of error in calculation of optical diffuse reflectance from turbid media using diffusion theory," Comput. Methods Program Biomed. **61,** 163–170 (2000).

23. L. H. Wang, S. L. Jacques, and L. Q. Zheng, "MCML—Monte Carlo modeling of photon transport in multi-layered tissues," Comput. Methods Program Biomed. **47,** 131–146 (1995).

24. T. J. Farrell, B. C. Wilson, and M. S. Patterson, "The use of a neural network to determine tissue optical properties from spatially resolved diffuse reflectance measurements," Phys. Med. Biol. **37,** 2281–2286 (1992).

25. H. C. van de Hulst, *Multiple Light Scattering* (Academic, New York, 1980), Vols. I and II.

26. R. Graff, J. G. Aarnoudse, F. F. M. de MulHenk, and W. Jentink, "Similarity relations for anisotropic scattering in absorbing media," Opt. Eng. **32,** 244–252 (1993).

27. J. S. Dam, T. Dalgaard, P. E. Fabricius, and S. Andersson-Engels, "Multiple polynomial regression method for determination of biomedical optical properties from integrating sphere measurements," Appl. Opt. **39,** 1202–1209 (2000).

28. W. F. Cheong and A. J. Welch, "A review of the optical properties of biological tissue," IEEE J. Quantum Electron. **26,** 2166–2185 (1990).

29. H. J. van Staveren, C. J. M. Moes, J. van Marle, S. A. Prahl, and M. J. C. van Gemert, "Light scattering in Intralipid-10% in the wavelength range of 400–1100 nm, " Appl. Opt. **30,** 4507–4514 (1991).

30. S. T. Flock, S. L. Jacques, B. C. Wilson, W. M. Star, and M. J. C. van Gemert, "Optical properties of Intralipid: a phantom medium for light propagation studies, " Lasers Surg. Med. **12,** 510–519 (1992).

31. S. J. Matcher, M. Cope, and D. T. Delpy, "Use of the water absorption spectrum to quantify tissue chromophore concentration changes in near-infrared spectroscopy," Phys. Med. Biol. **39,** 177–196 (1994).

32. J. R. Mourant, I. J. Bigio, D. A. Jack, T. M. Johnson, and H. D. Miller, "Measuring absorption coefficients in small volumes of highly scattering media: source–detector separations for which path lengths do not depend on scattering properties," Appl. Opt. **36,** 5655–5661 (1997).

33. G. Kumar, "Optimal probe geometry for near-infrared spectroscopy of biological tissue," Appl. Opt. **36,** 2286–2293 (1997).

34. C. R. Simpson, M. Kohl, M. Essenpreis, and M. Cope, "Near-infrared optical properties of *ex vivo* human skin and subcutaneous tissues measured using the Monte Carlo inversion technique," Phys. Med. Biol. **43,** 2465–2478 (1998).

35. F. P. Bolin, L. E. Preuss, R. C. Taylor, and R. J. Ference, "Refractive index of some mammalian tissues," Appl. Opt. **28,** 2297–2303 (1989).